A Closed-loop System for Resonant MEMS Sensors Subject to Blue-sideband Excitation

Lei Xu, Jingqian Xi, Lu Gao, Fangzheng Li, Jianyuan Pi, Chengxin Li, Kunfeng Wang, Xingyin Xiong,
Yuan Wang, Huafeng Liu, Xudong Zou, Chun Zhao, *Senior Member*

***Abstract*—his studyhis studyT reports a closed-loop system (CLS) for resonant micro-electromechanical systems (MEMS) sensors subject to blue-sideband excitation (BSE) for the first time. Compared with the conventional excitation scheme, which uses an AC signal with a frequency that is very close to or equal to that of the desired MEMS resonator mode, the BSE scheme applies an AC signal with a frequency equal to or near the sum of two resonant frequencies to excite the resonator. This requires a CLS to provide a sum-frequency excitation signal to serve as the resonator's feedback driving signal for practical applications. The proposed CLS mainly consists of a digital lock-in amplifier (DLA), a phase-locked loop (PLL) and a BSE control module (BSE-CM), and is implemented using a field-programmable gate array (FPGA). Experiments showed that the system can track the combined frequency of two flexural modes of the resonator in real-time. In addition, a potential application of the CLS for resonant MEMS sensors subject to BSE is preliminarily demonstrated, showing that the sensitivity of a vacuum-packaged resonant MEMS accelerometer can be enhanced by 166%. This approach could also be applied to reduce the effects of the feedback phase, or to simultaneously monitor multiple parameters. This study represents critical progress for practical sensing using the BSE scheme.**

***Index Terms*—MEMS resonant sensor, oscillator, sensitivity enhancement, blue-sideband excitation, FPGA.**

I. INTRODUCTION

MEMS resonators are increasingly employed as the key sensing element for high-precision sensors, including accelerometers [2]–[5], gyroscopes [6]–[8], pressure sensors [9], [10], magnetometers [11], [12] and thermometers [13], [14]. These sensors are usually implemented using a frequency-modulated (FM) readout to achieve a high stability performance [15]. The MEMS resonators must be driven into resonance for these sensors to work properly, and the driving frequency must be modified in real-time when the measurand changes in value. Therefore, a closed-loop system (CLS) that automatically generates an appropriate excitation frequency is indispensable for practical applications of such a resonant sensor.

Up to this point, virtually all resonant sensors employ a type of system that automatically generates an excitation frequency equal to the vibration mode, which can be the fundamental mode [16] or other modes [17]. With this configuration, the drive signal has the same frequency as the frequency of the motional current generated by the resonator. The operation of this type of CLS [15], [18] requires that the Barkhausen criterion for oscillations is satisfied [19]. The output frequency depends on the feedback phase due to the phase condition of the Barkhausen criterion. Parametric oscillators, in which parametric excitation at twice the resonant frequency is applied, also exist in the literature [20]. This topology is advantageous in terms of minimum cross-talk, nonlinear properties control, large frequency tunability, and significant phase-noise reduction. However, the frequency-phase dependence (14 kHz/deg) is a drawback in this topology. This frequency-phase dependence is one of the limiting factors of readout noise for resonant MEMS sensors [21], [22].

Recently, optomechanical self-oscillations, as well as micro- and nanoelectromechanical system (MEMS/NEMS) resonators subject to blue-sideband excitation (BSE) have attracted research interest from the community [23]–[32]. The resonator can be excited by applying a signal that periodically modulates the resonator's stiffness, at a frequency equal to the sum of two modal frequencies. Frequency-phase sensitivity can be eliminated with this excitation method compared with the conventional approach [27]. This advantage of the BSE scheme allows the improvement of the resonant sensor performance. Finally, two modes can be simultaneously excited using the BSE approach [28]. This can be useful for achieving simultaneous multiple-input monitoring, or frequency synthesizer applications [33]. However, there are few reports on closed-loop readout systems for resonant MEMS sensors subject to BSE despite their interesting properties.

This study proposes a closed-loop control and readout system for a prototype resonant MEMS sensor subject to BSE and implements it based on an off-the-shelf field-programmable gate array (FPGA). The all-digital control system, consisting of a lock-in amplifier, phase-locked loop, and BSE control

---

This article is extended from a paper presented at the 2022 The 35th International Conference in MEMS [1].

L. Xu, J. Xi, L. Gao, F. Li, J. Pi, C. Li, Y. Wang, H. Liu and C. Zhao are with MOE Key Laboratory of Fundamental Physical Quantities Measurement and Hubei Key Laboratory of Gravitation and Quantum Physics, PGMF and School of Physics, Huazhong University of Science and Technology, Wuhan, China, 430074.

K. Wang, X. Xiong and X. Zou are with The State Key Laboratory of Transducer Technology, Aerospace Information Research Institute, Chinese Academy of Sciences, Beijing, China, 100190.

X. Zou is also with School of Electrical and Communication Engineering, University of Chinese Academy of Sciences, Beijing, China, 100049, and QiLu Aerospace Information Research Institute, Chinese Academy of Sciences, Jinan, China, 250100.

C. Zhao is also with Department of Electronics Engineering, University of York, Heslington, York, UK, YO10 5DD.

This work is supported in part by the National Key Research and Development Program of China, grant No. 2018YFB2002300, and in part by the"Fundamental Research Funds for the Central Universities", HUST, grant No.: 2019kfyXJJS157.

L. Xu and J. Xi contributed equally in this work.

Corresponding author: Yuan Wang, yuan_wang@hust.edu.cn.

module, can track the combined frequency of two flexural modes of the resonator in real-time. It can also produce a frequency output equal to the sum of two modal frequencies. This could potentially be useful for enhancing the sensitivity of a resonant MEMS sensor. Further, as a proof-of-concept, the sensitivity enhancement is preliminarily demonstrated using a vacuum packaged resonant MEMS accelerometer in this study. This represents a first step toward employing BSE for practical resonant MEMS sensor applications, which could help reduce the effects of the feedback phase, enhancing the sensitivity of resonant MEMS sensors, or multiparameter monitoring.

II. BLUE-SIDEBAND EXCITATION

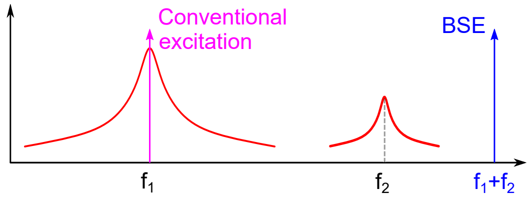

Fig. 1: Illustration of the blue-sideband excitation (BSE) scheme, where only the excitation signal near the sum of two resonant frequencies is applied.

Instead of conventional driving where the excitation signal is near the fundamental mode, blue-sideband excitation (BSE) applies an AC signal with a frequency near the sum of two modes of the resonator [29] (Fig. 1). Based on our previous derivation [13], the dynamics of the first two modes subject to only BSE can be expressed as follows:

$$\begin{aligned} &m_1\ddot{u_1}+c_1\dot{u_1}+k_1u_1\\ &+k_{n1}u_1^3+k_{n2}u_1^2u_2+k_{n3}u_1u_2^2+k_{n4}u_2^3\\ &=k_{c1}u_2+\lambda_1\cos(2\pi f_{\mathrm{BSE}}t)u_1+\Lambda_1\cos(2\pi f_{\mathrm{BSE}}t)u_2 \end{aligned} \tag{1}$$

$$\begin{aligned} &m_2\ddot{u_2}+c_2\dot{u_2}+k_2u_2\\ &+k_{n5}u_2^3+k_{n6}u_2^2u_1+k_{n7}u_2u_1^2+k_{n8}u_1^3\\ &=k_{c2}u_1+\lambda_2\cos(2\pi f_{\mathrm{BSE}}t)u_2+\Lambda_2\cos(2\pi f_{\mathrm{BSE}}t)u_1 \end{aligned} \tag{2}$$

where m_r, c_r, k_r, k_{cr}, λ_r, and Λ_r represent the effective mass, damping, effective stiffness, inter-modal coupling stiffness, pumping coefficient, and inter-modal pumping coefficient for the rth mode ($r=1$ and 2), respectively. k_{nj} ($j=1,2,...,$ and 8) denote the corresponding nonlinear stiffness. The equations can be numerically solved using the method of multiple scales [34]. Previous solutions to a similar problem [35] showed that when $f_{\mathrm{BSE}}\approx f_1+f_2$, numerical solutions of u_1 and u_2 exist simultaneously; therefore, both modes 1 and 2 can be excited by the BSE signal. The term 'blue-sideband' is used here, which is contrary to recent studies of parametric modulation using a red-sideband modulation signal, $f_{\mathrm{red}}\approx f_2-f_1$ [36]–[38], in which energy is transferred between the two modes. The blue-sideband signal can pump energy from the mechanical cavity into both modes [32], thereby simultaneously exciting modes 1 and 2.

In addition, this excitation scheme is distinguishable from conventional driving, where the readout frequency is f_1 or f_2 and the excitation frequency is f_{BSE}.

III. CLOSED-LOOP SYSTEM FOR A GENERIC RESONATOR

A. Device description

This section describes a closed-loop control system for a generic resonator. The resonator used in this study is a clamped-clamped beam resonator (Fig. 2a), which is fabricated using a commercially available SOIMUMPS process provided by MEMSCAP. The dimensions of the resonator are $800\times8\times25\mu\mathrm{m}^3$ (length × width × thickness).

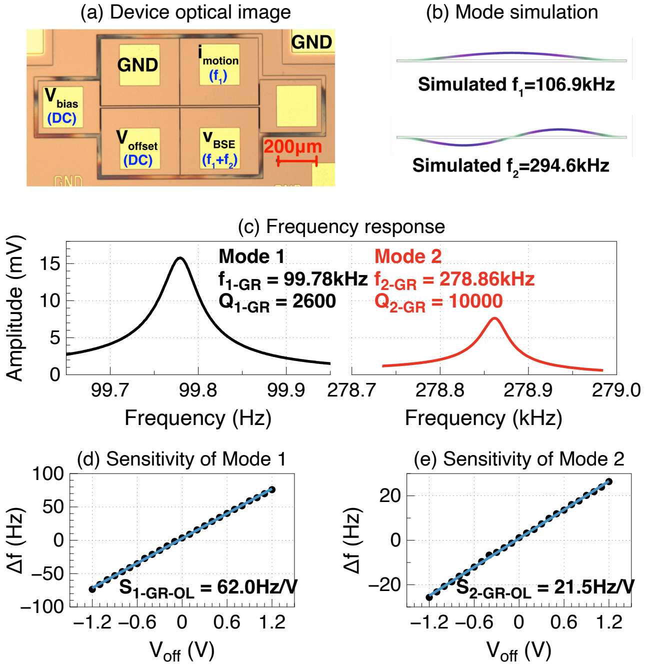

Fig. 2: (a) Optical image of the clamped-clamped beam resonator used in this study; (b) simulated mode shapes and frequencies of the resonator's first two modes; (c) measured frequency responses of the first two modes of the resonator; (d) measured sensitivity of mode 1 frequency with respect to offset voltage changes; (e) measured sensitivity of mode 2 frequency with respect to offset voltage changes.

The modes of interest here are the resonator's first two in-plane flexural modes. Fig. 2b shows the simulated mode shapes and frequencies of these two modes. Fig. 2c shows the measured frequency responses, and extracted resonant frequencies (f_1=99.78 kHz and f_2=278.86 kHz, respectively) and quality factors (Q_1=2600 and Q_2=10000, respectively).

The resonator can also be used as a prototype sensor, as its resonant frequencies change when a DC offset voltage is applied to one of the electrodes (Fig. 2a). This property can be used to mimic the typical behavior of a resonant MEMS sensor subject to stiffness perturbations. Measured sensitivities of each of the first two modes with respect to the applied offset voltage are S_1=62.0 Hz/V and S_2=21.5 Hz/V, respectively, (Fig. 2d and Fig. 2e).

B. Closed-loop system design

To implement the feedback control loop, conventional MEMS oscillators use a phase feedback approach to lock to the

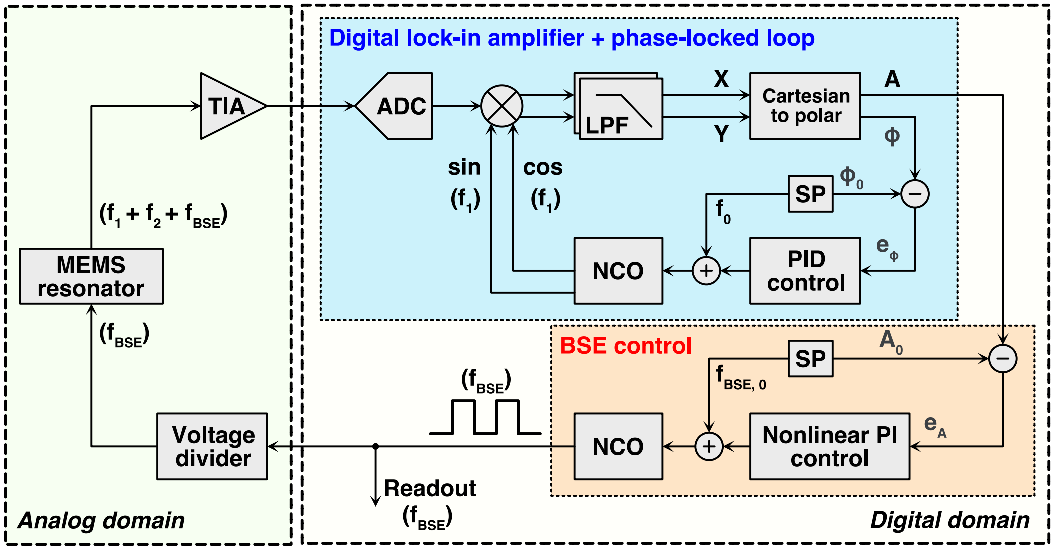

Fig. 3: Detailed block diagram of the closed-loop system (CLS), consisting of DLA, PLL, and BSE control modules.

resonant frequency. However, the BSE response is independent of the excitation signal's phase. Thus, using other methods to achieve and sustain oscillations is critical.

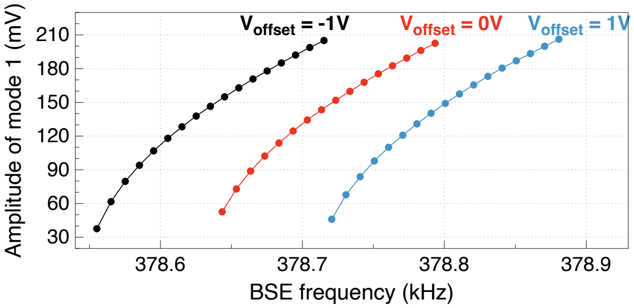

Fig. 4: Measured amplitude of the first mode with respect to blue-sideband excitation (BSE) frequency, with different offset voltages, V_{offset}.

Previous solutions to a problem similar to Equations 1 and 2 show that the solution u_1 is a function of the BSE frequency f_{BSE} [35]. This is demonstrated in the experiment results (Fig. 4). The amplitude control approach is employed to achieve and sustain oscillations based on this observation.

The CLS is designed to function as follows. Initially, the numerically controlled oscillator (NCO) generates a frequency, $f_0 = f_{\text{BSE},0}$ near the sum of the two modal frequencies. With this BSE signal, the MEMS resonator responds and produces a motional current containing three frequency components (mainly at f_1 and f_2, in addition to feedthrough at f_{BSE}). When the amplitude of mode 1 is different from an amplitude setpoint (SP), A_0, a control scheme in the feedback loop produces a change in the BSE frequency, which automatically corrects the deviation from the SP value (Fig. 4). Thus, the feedback loop can automatically produce a BSE frequency to sustain the oscillation, with the amplitude of mode 1 sustained at A_0.

Similarly, by introducing an external perturbation, the feedback loop detects the amplitude deviation from the SP A_0 (see Fig. 4) and responds with a change in BSE frequency to maintain the same vibrational amplitude, thereby tracking the frequency changes.

To achieve these desired functionalities, the system implementation is described in the following sections.

1) System overview: The CLS based on BSE is essentially a two-stage feedback control system (Fig. 3). The first stage is the phase-locked loop (PLL), which is designed to lock to the resonator's first mode (f_1) and extract the amplitude of mode 1 (A), among other frequency components. The PLL also contains a digital lock-in amplifier (DLA). The most challenging part of the proposed CLS compared with that of a parametric oscillator [20], [39] is the amplitude control in the second loop, which is realized in the second-stage BSE control block. In the second stage, the extracted amplitude is compared with the amplitude SP (A_0), generating a digital control signal for the NCO based on Fig. 4. The NCO produces a square wave signal with a frequency of f_{BSE}, which is used to excite the MEMS resonator. In this study, the PLL, DLA and BSE controls are implemented using a commercially available Xilinx AX7102 FPGA.

In addition to the digital circuits, the analog part of the CLS, consisting of a transimpedance amplifier (TIA) and a voltage divider is also essential. The detailed design of the CLS is described below.

2) Analog-to-digital converter (ADC): To enable the FPGA for subsequent signal processing, an ADC is employed to digitize the analog voltage signal from the TIA. In this study, an off-the-shelf 16-bit high-speed ADC (LTC2204, Analog Devices Inc.), with an optional full-scale input range of 2.25 $V_{\text{P-P}}$ and a maximum sampling rate of up to 40 MHz, is used as a standalone ADC, rather than the integrated 12-bit ADC in the FPGA for improved noise performance. The selected ADC is sufficient for this proof-of-concept work, in which the sampling rate and bit width are capable of processing the dynamic signals in this study (frequency in the 100 kHz range, and amplitude in the range of 100 mV). If the signal-to-be-processed has a higher frequency, or if low-noise performance is required, ADCs with larger bit width and higher sampling rate would be necessary.

3) PLL and DLA: A PLL is required to extract the signal of the first flexural mode (f_1) from the other frequency components (predominantly f_2 and f_{BSE}).

In the PLL, a DLA is employed to act as the phase detector, to extract the phase difference (Φ) between the f_1 component within the resonator output signal and the reference signals. The DLA approach can obtain the amplitude information compared with other phase detectors, such as XOR gates [40] and hybrid-phase frequency detectors (PFD) [41]. By multiplying the input signal with a pair of quadrature reference signals, and then passing the output of the mixer through a low-pass filter, the in-phase and quadrature components (X and Y, respectively) can be obtained. The amplitude A and the phase Φ can be derived by converting the Cartesian coordinates into polar coordinates using the following relationship:

$$A = \sqrt{X^2 + Y^2} \tag{3}$$

$$\Phi = \operatorname{atan2}(Y, X) \tag{4}$$

Here, the $atan2$ function is used rather than the $atan$ function, to expand the phase-detection range to $(-\pi, \pi]$.

The phase information is then fed to a PID controller and an NCO, which acts as the voltage-controlled oscillator (VCO) in the PLL. The PLL is capable of locking to the f_1 component by setting the reference signals near the first modal frequency, $f_1 \approx$100 kHz. Notably, since the PLL is implemented based on the FPGA, it can also be easily configured to extract the frequency component at f_2 if necessary.

To achieve high-resolution frequency generation, the clock frequency used here is f_{clk} =20 MHz, and the bit width of the phase accumulator is N =40 bits. With these parameters, the theoretical frequency resolution of the NCO can reach $f_{\mathrm{clk}}/2^N = 18\ \mu$Hz.

The lock-in approach as a phase detector has the additional advantage of filtering out undesired signals and noise. The bandwidth of the low-pass filter is set to 1 kHz in this prototype system to balance the response speed and precision. The bandwidth can be tuned accordingly for high-precision or high-speed applications, due to the digital nature of the system. However, the inaccuracies and noise added in the amplitude demodulation process could be a contributing factor to the system total instability and noise.

4) BSE control: The amplitude of the first mode is fed into the BSE control to generate a BSE signal based on the amplitude and BSE frequency relationship shown in Fig. 4. By comparing the amplitude to a setpoint (SP), A_0, the excitation frequency is adjusted so that the amplitude of the first mode is maintained at A_0. In this proof-of-concept work, the amplitude SP is arbitrarily chosen as $A_0 = 173$ mV. This parameter can be easily adjusted based on different requirements, considering the digital nature of the control circuit.

A square wave excitation signal with 3.3 $\mathrm{V_{P-P}}$ is generated by the NCO, and is then attenuated to V_{BSE} =2.5 $\mathrm{V_{P-P}}$ through a voltage divider. This attenuated square wave signal ultimately becomes the driving signal for the BSE scheme. To begin the oscillation, an initial BSE frequency of $f_{\mathrm{BSE},0} = 378.77$ kHz is generated using the NCO, which ensures that the resonator is excited. Thereafter, the feedback control loop starts to function, and the BSE frequency is adjusted, maintaining the amplitude of the resonator in the first mode at 173 mV. Because the NCO in the second loop has the same clock frequency and phase accumulator width as the NCO in the PLL, the same frequency step resolution of 18 μHz can be achieved. The quality of the NCO output signal also depends on the quality of the clock signal. Therefore, to minimize the noise, selecting clocks with high stability, accuracy, and low jitter is recommended. Therefore, an external high-resolution clock generator is used rather than the embedded clock generator in the FPGA board. In addition, the clock generator could be a contributing factor to the system's total power consumption. In low-power applications, selecting a low-power clock generator, such as a MEMS-based clock generator, is necessary.

The parameters used in the CLS are presented in Table I.

TABLE I: Parameters used in the closed-loop system (CLS) design

Parameters	Values
System sample frequency	20 MHz
ADC sample frequency	20 MHz
Clock of NCO	20 MHz
LPF bandwidth	1 kHz
f_0	99.8 kHz
Φ_0	0 deg
A_0	173 mV
$f_{\mathrm{BSE},0}$	378.77 kHz
V_{BSE}	2.5 $V_{\mathrm{P-P}}$
Phase accumulator width	40 Bit

C. Experimental results

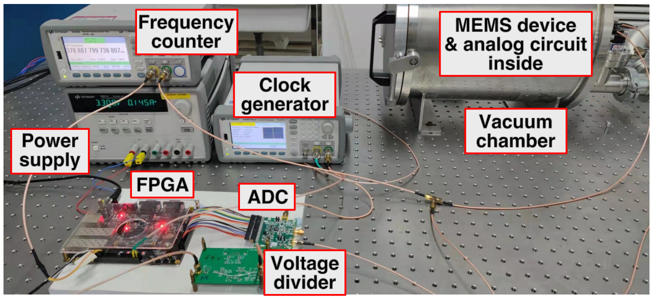

Fig. 5: Demonstration of the implemented closed-loop system (CLS) for the generic clamped-clamped beam type resonator.

The CLS is designed and implemented using the parameters above, achieving self-sustained oscillations. Thereafter, an additional offset voltage V_{offset} is introduced to perturb the resonator to verify the system's dynamic functionality.

A commercially available lock-in amplifier (MFLI, Zurich Instruments) is connected to the output of the TIA to monitor the mode frequency and amplitude of the resonator's first mode. The MFLI lock-in amplifier is not necessary for the CLS implementation; however, it is added here merely to monitor the first mode to ensure proper CLS operation. In addition, a frequency counter (53230A, Keysight) is employed to measure the changes in BSE excitation frequency f_{BSE}. Fig. 6 shows the measured results.

(a) Mode 1 frequency and amplitude

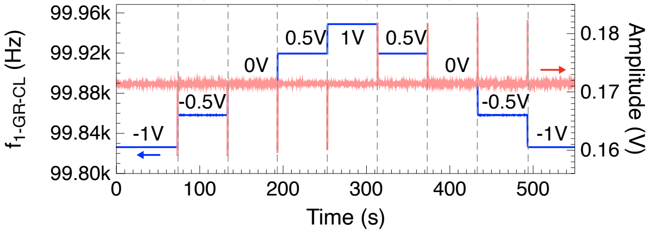

(b) pump frequency

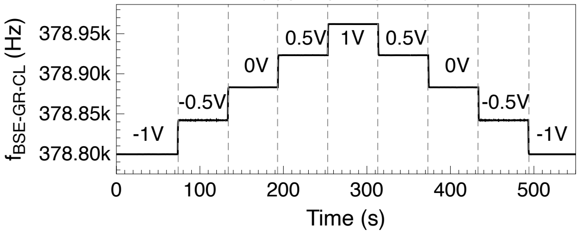

Fig. 6: (a) Measured response of the resonator's first mode, when an offset voltage ranging from -1 V to 1 V is changed in steps. The frequency changes are shown in blue and amplitude changes are shown in red ($f_{1-\mathrm{GR-CL}}$ represents the first mode frequency of the generic resonator under test, with the closed-loop configuration); (b) the simultaneously measured results of the blue-sideband excitation (BSE) frequency ($f_{\mathrm{BSE-GR-CL}}$ represents the blue-sideband excitation frequency of the generic resonator under test, with the closed-loop configuration).

Fig. 6a shows that when the DC offset voltage V_{offset} changes in steps from -1 V to 1 V and back, the prototype sensor's first modal frequency changes accordingly. The insignificant discrepancies between the measured frequency and the first mode frequency (Fig. 2c) may be due to frequency drifts between measurements.

Meanwhile, the amplitude of the first mode is maintained at an amplitude of approximately 171 mV due to the CLS. The spikes in amplitude represent the transients of the CLS responding to the sudden V_{offset} changes. The CLS is capable of controlling the amplitude as anticipated, except for a slight discrepancy between measured amplitude and the SP, which may be due to a mismatch between the two voltage references in the FPGA and MFLI.

Fig. 6b shows that the BSE signal's frequency is close to the sum of two resonant frequencies as designed. Further, the BSE bidirectional changes in offset voltage do not result in significant hysteresis in BSE frequencies. These characteristics make the CLS suitable for sensing and timing reference applications.

In addition, it is also expected that $\Delta f_{\mathrm{BSE}} = \Delta f_1 + \Delta f_2$. To verify this, the sensitivity of the BSE frequency, f_{BSE} with respect to V_{offset} is characterized. The results are shown in Fig. 7. The extracted sensitivity is S_{BSE} =82.5 Hz/V. Fig. 2d and Fig. 2e show that the measured sensitivities of each of the first two modes with respect to this offset voltage are S_1=62.0 Hz/V and S_2=21.5 Hz/V, respectively. Therefore, the conclusion of $S_{\mathrm{BSE}} = S_1 + S_2$ can be drawn. This confirms the proper functionality of the CLS. In addition, another advantage of the CLS based on BSE scheme, which is its capability of improving the sensitivity of resonant MEMS sensors, is demonstrated.

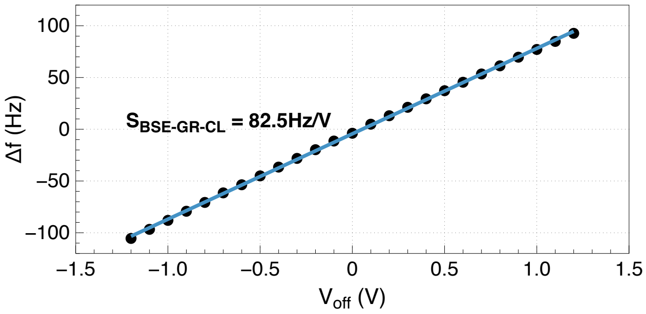

Fig. 7: Measured sensitivity of the blue-sideband excitation (BSE) frequency with respect to offset voltage changes ($S_{\mathrm{BSE-GR-CL}}$ represents the blue-sideband excitation sensitivity of the generic resonator under test, with the closed-loop configuration).

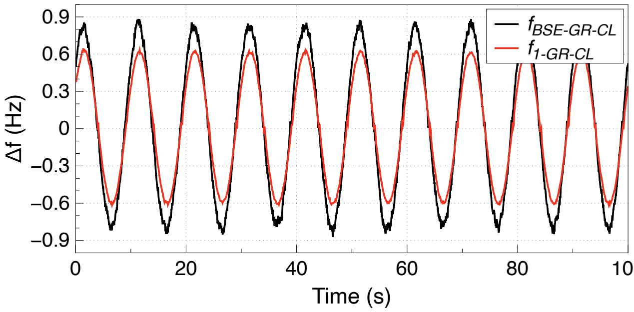

Fig. 8: Measured dynamic response of f_{BSE} (in black) and f_1 (in red) after introducing a dynamic stiffness perturbation signal, f_{offset}=0.1 Hz ($f_{1-\mathrm{GR-CL}}$ and $f_{\mathrm{BSE-GR-CL}}$ represents the first mode frequency and the blue-sideband excitation frequency of the generic resonator under test, with the closed-loop configuration, respectively).

Next, the dynamic response of the CLS is characterized. For this test, a periodically modulated offset voltage signal, with v_{offset}=10 mV and f_{offset}=0.1 Hz, is applied to the resonator to generate a dynamic stiffness perturbation. Fig. 8 shows the measured results. The changes in f_{BSE} are capable of tracking the periodic change at a frequency of 0.1 Hz. This represents additional evidence of the CLS's full functionality. This measurement demonstrates that measuring the changes in f_{BSE} is beneficial for improving the resonant MEMS sensor's sensitivity.

IV. CLOSED-LOOP SYSTEM FOR A RESONANT MEMS ACCELEROMETER

The CLS can enhance the sensitivity of a resonant MEMS accelerometer, based on previous demonstrations. To conduct a preliminary investigation of this idea, the CLS parameters are adjusted to work with a wafer-level vacuum-encapsulated resonant MEMS accelerometer, whose design is described in detail elsewhere [4].

Fig. 9a and Fig. 9b show the open-loop frequency responses of the sensing resonator's first two flexural modes, without any acceleration input. The resonant frequencies are 196.94 kHz and 393.82 kHz, and the extracted Q-factors are approximately 57000 and 36000, for the first and the second mode respectively. The accelerometer's sensitivity is characterized using a standard tilt test with the open-loop configuration. In addition, Fig. 9c and Fig. 9d show that the measured sensitivity of the first two flexural modes are 456.1 Hz/g and 752.9 Hz/g, respectively.

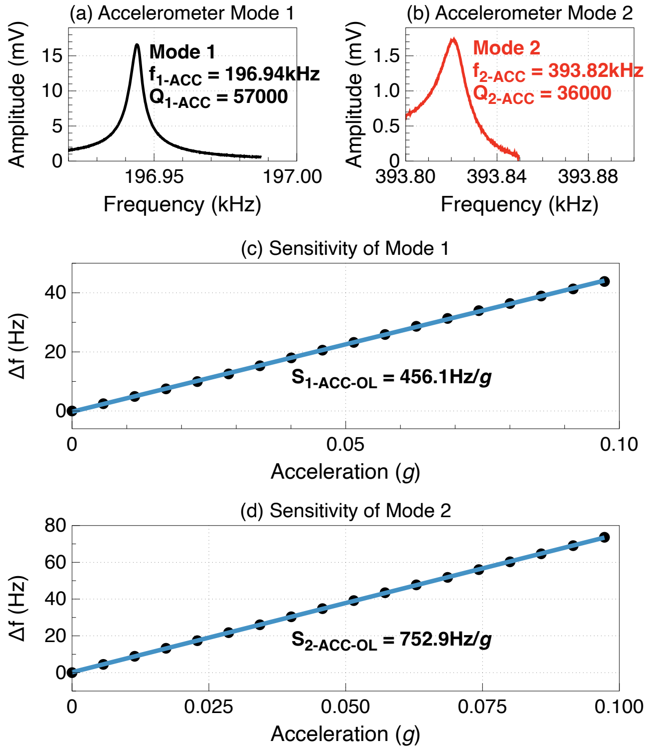

Fig. 9: Measured frequency response of (a) the first flexural mode, and (b) the second flexural mode, using an open-loop configuration. The measured sensitivity of (c) the first flexural mode, and (d) the second flexural mode, based on a tilt test with an open-loop configuration.

Subsequently, the parameters are adjusted to implement the CLS for the resonant accelerometer. Particularly, the f_0, A_0 and $f_{\mathrm{BSE},0}$ values are adjusted, whereas all other parameter values remain the same (Table II). Fig. 10 shows the measured amplitude of the first mode with respect to the BSE frequency. The nonlinear PI control function is also changed based on the measurements.

The oscillation can be initiated and sustained for the resonant accelerometer based on the aforementioned CLS design.

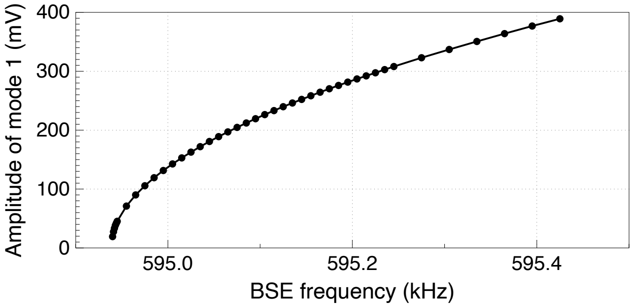

Fig. 10: Measured amplitude of the first mode with respect to blue-sideband excitation (BSE) frequency for the resonant MEMS accelerometer.

TABLE II: Parameters used in the closed-loop system (CLS) design for the resonant accelerometer

Parameters	Values
System sample frequency	20 MHz
ADC sample frequency	20 MHz
Clock of NCO	20 MHz
LPF bandwidth	1 kHz
f_0	195.8 kHz
Φ_0	0 deg
A_0	175 mV
$f_{\mathrm{BSE},0}$	595.06 kHz
V_{BSE}	2.5 $V_{\mathrm{P-P}}$
Phase accumulator width	40 Bit

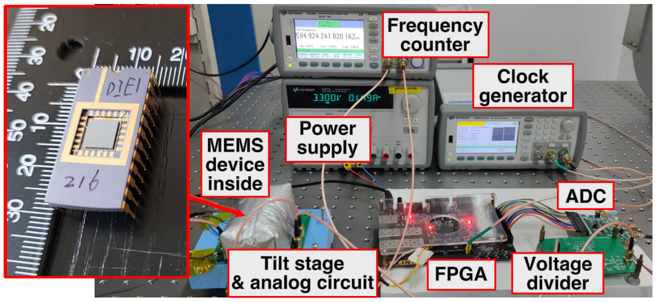

Fig. 11: Demonstration of the implemented closed-loop system (CLS) for the vacuum-packaged resonant MEMS accelerometer, as shown on the inset.

Closed-loop sensitivity of the accelerometer can also be characterized, using a similar experimental setup as the generic resonator. The vacuum chamber was not used here since the accelerometer under-test is vacuum packaged. Thermal insulation and an active temperature controller are used to minimize the effect of ambient temperature fluctuations. The acceleration change is introduced using a tilt table, which is placed beneath a thick layer of vibration isolation foam attached to the analog circuit for the MEMS device. Fig. 11 shows the experimental setup.

The sensitivity of the resonant accelerometer can be characterized in a closed-loop configuration using the CLS with the aid of an external MFLI lock-in amplifier. The extracted sensitivity for the first mode is $S_{1-\mathrm{ACC-CL}} = 457.1$ Hz/g,

(a) Sensitivity of Mode 1

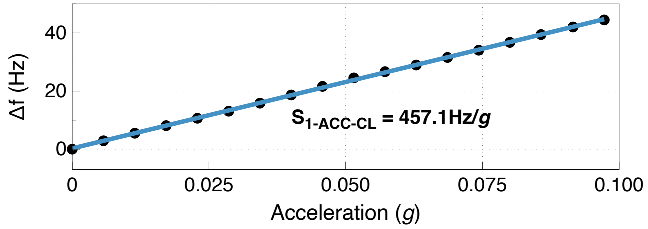

(b) Sensitivity of BSE frequency

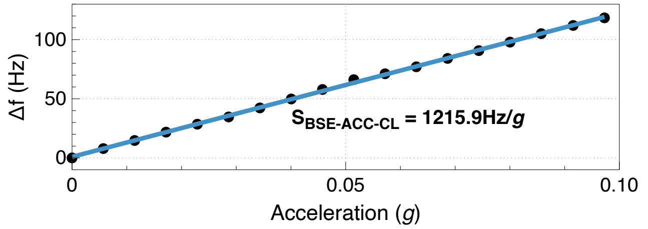

Fig. 12: Measured sensitivity of (a) Mode 1 and (b) blue-sideband excitation (BSE) frequency in the closed-loop configuration.

as shown in Fig. 12a, which is consistent with the open-loop sensitivity of $S_{1-\mathrm{ACC-OL}} = 456.1$ Hz/g, with an error of 0.2%. This shows the proper operation of the CLS.

The closed-loop sensitivity, $S_{\mathrm{BSE-ACC-CL}} = 1215.9$ Hz/g can be extracted by measuring the frequency changes at the CLS output. This is also consistent with the sum of open-loop sensitivity, which is approximately 1209 Hz/g. The output sensitivity can be enhanced by 166% when the CLS is implemented compared with the conventional closed-loop readout system, in which the first mode is typically tracked.

V. DISCUSSION

A. *Noise discussion*

The noise performance of the CLS is also characterized, and compared with the noise floor of the conventional oscillator configuration obtained using similar vibration amplitudes. For discussion, it is desired to exclude the effects of ambient vibration; therefore, only the result from the clamped-clamped beam is presented in Fig. 13. The measurement results show that the noise performance of our CLS is worse, particularly in the low-frequency part, compared with the conventional oscillator configuration. Further, some of the low-noise resonator sensors reported so far can reach the level of tens $\mu\mathrm{Hz}/\mathrm{Hz}^{1/2}$ in the vicinity of 10 Hz bandwidth [42]–[44], which is superior to our results. Through our analysis, the additional noise likely comes from a few factors discussed below; therefore, to improve the noise performance of the proposed closed-loop system, the following aspects should be addressed in the future.

First of all, improving the oscillation amplitude SP A_0 does not significantly improve the noise performance (Fig. 14). Therefore, it is speculated that most of the additional noise may be attributed to the amplitude-to-frequency conversion (Fig. 4). This problem can be solved by reducing the amplitude noise entering the BSE control module, such as employing an ADC with higher precision, reducing the bandwidth of the DLA and PLL, or adding more digital filters for the amplitude.

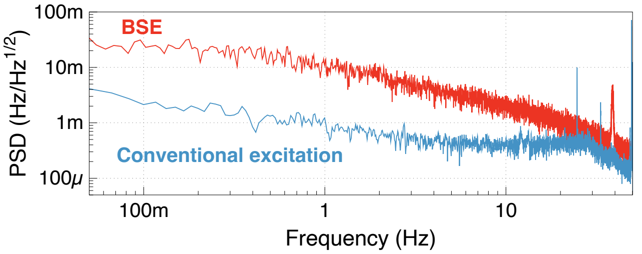

Fig. 13: Measured PSD of the clamped-clamped beam using the closed-loop system (CLS) (in red) and the conventional oscillator setup (in blue), with similar vibration amplitude in both cases.

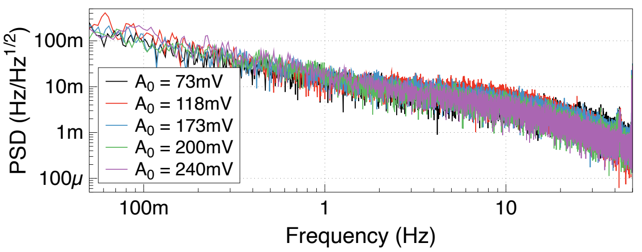

Fig. 14: Measured PSD of the clamped-clamped beam using the closed-loop system (CLS) with different oscillation amplitude SPs A_0.

From our experience in designing and optimizing the system, we propose that the most effective method for addressing this problem is to optimize the MEMS structures and/or dynamics, to obtain a low amplitude-to-frequency conversion slope, which is ideally close to a vertical line in Fig. 4.

The system noise may also be attributed to the inaccuracies of the demodulator, which is not typically used in the conventional oscillator. The amplitude produced from the demodulator is critical to the output frequency noise, as discussed above. To reduce the system noise from the demodulator, further investigations on the underlying mechanisms, and optimization of the demodulator structure will be necessary for future studies.

Furthermore, the additional noise can be attributed to DC bias-voltage-to-frequency conversion, since this conversion ratio is increased by employing the CLS. This can be solved by employing a low-noise DC bias voltage source. Other noise deterioration factors can include undesired ground loops, which can be solved by integrating all systems onto a single mixed-signal board.

B. *Other sensors, structures and modes*

Modal interaction, or coupling, is critical for devices to operate with the BSE scheme. Therefore, resonant sensors that benefit from this scheme would require the presence of modal coupling. This can include a capacitively transduced clamped-clamped beam as a thermometer [13], single-ended or double-ended tuning forks based sensors such as pressure sensors [45] and magnetometers [46]. Capacitively transduced ring resonators also exhibit similar modal interactions [36]; therefore, such an approach should also apply to gyroscopes with similar structures [6], [47]. Previous experimental evidence shows that nonlinear modal coupling exists in bulk mode resonators [48]; therefore, it is believed that sensors based on these resonators can be used. Recently reported resonant sensor devices, such as mass sensors [49], based on two or more weakly coupled resonators [50]–[53], can also benefit from this scheme. In this study, the first two modes of the clamped-clamped beam resonator are used. However, this approach is not necessarily limited to these two modes. Implementing the CLS should be possible as long as there is sufficiently strong modal coupling between other modes, such as a cantilever-beam type resonator through the coupling between flexural and extensional bulk modes [54]. However, to practically use other structures, more investigations into the underlying coupling mechanism, and experimental verification are necessary.

VI. CONCLUSION

This study presents a CLS for resonant MEMS sensors subject to BSE for the first time. The CLS mainly consists of a digital control system implemented based on a commercially available FPGA. We demonstrated that the proposed CLS is capable of capturing dynamic frequency changes in real-time, making the system suitable for practical sensing applications. A potential application of the CLS is also preliminarily demonstrated, which is to improve the sensitivity of a vacuum-packaged resonant MEMS accelerometer. Because the output sensitivity of the CLS approximately equals the sum of the sensitivity of the two fundamental modes of the resonator, experimental results show that the sensitivity of the resonant MEMS accelerometer was enhanced by 166%, compared with a common AC drive scheme.

This study represents an important first step toward employing BSE for practical resonant MEMS sensor applications, which can be a viable alternative to existing oscillator topologies. The CLS described in this study enhances the sensitivity of resonant sensors. The interesting property of the feedback phase independence can also be explored. Furthermore, employing BSE and the proposed CLS can also be useful for simultaneous multiparameter monitoring, since various modal information can be extracted concurrently from the system. However, compared with the existing oscillator topologies, the noise performance and power consumption could be current limiting factors of the CLS. Therefore, future studies should focus on optimization of the design of the entire system, from the resonator to each system module, to improve the overall system's performance, such as noise and power consumption.

REFERENCES

[1] L. Xu, L. Gao, J. Xi, F. Li, J. Pi, C. Li, Y. Wang, H. Liu, and C. Zhao, "A low-noise frequency readout system for blue-sideband excited resonant MEMS sensors," in *2022 IEEE 35th International Conference on Micro Electro Mechanical Systems Conference (MEMS)*, 2022, pp. 810–813.

[2] G. Sobreviela-Falces, M. Pandit, A. Mustafazade, C. Zhao, C. Pili, C. Baker, and A. Seshia, "A MEMS Vibrating Beam Accelerometer for High Resolution Seismometry and Gravimetry," in *2021 IEEE 34th International Conference on Micro Electro Mechanical Systems (MEMS)*. Gainesville, FL, USA: IEEE, Jan. 2021, pp. 196–199.

[3] T. Miani, T. Verdot, A. Berthelot, F. Maspero, A. Koumela, P. Robert, G. Langfelder, J. Arcamone, and M. Sansa, "Resonant Accelerometers Based on Nanomechanical Piezoresistive Transduction," in *2021 IEEE 34th International Conference on Micro Electro Mechanical Systems (MEMS)*. Gainesville, FL, USA: IEEE, Jan. 2021, pp. 192–195.

[4] X. Xiong, X. Zou, Z. Wang, K. Wang, Z. Li, and W. Yang, "Using Electrostatic Spring Softening Effect to Enhance Sensitivity of MEMS Resonant Accelerometers," *IEEE Sensors Journal*, vol. 21, no. 5, pp. 5819–5827, Mar. 2021.

[5] S. Shin, H.-K. Kwon, G. D. Vukasin, T. W. Kenny, and F. Ayazi, "A temperature compensated biaxial eFM accelerometer in Epi-seal process," *Sensors and Actuators A: Physical*, vol. 330, p. 112860, Oct. 2021.

[6] Q. Li, D. Xiao, X. Zhou, Y. Xu, M. Zhuo, Z. Hou, K. He, Y. Zhang, and X. Wu, "0.04 degree-per-hour MEMS disk resonator gyroscope with high-quality factor (510 k) and long decaying time constant (74.9 s)," *Microsystems & Nanoengineering*, vol. 4, no. 1, p. 32, Dec. 2018.

[7] M. Hodjat-Shamami and F. Ayazi, "Eigenmode operation of piezoelectric resonant gyroscopes," *Microsystems & Nanoengineering*, vol. 6, no. 1, p. 108, Dec. 2020.

[8] Y. Wang, Y.-W. Lin, J. Glaze, G. D. Vukasin, D. D. Shin, H.-K. Kwon, D. B. Heinz, Y. Chen, D. D. Gerrard, T. W. Kenny, and A. M. Shkel, "Quantification of Energy Dissipation Mechanisms in Toroidal Ring Gyroscope," *Journal of Microelectromechanical Systems*, vol. 30, no. 2, pp. 193–202, Apr. 2021.

[9] Y. Li, Y. Lu, B. Xie, J. Chen, J. Wang, and D. Chen, "A Micromachined Resonant Differential Pressure Sensor," *IEEE Transactions on Electron Devices*, vol. 67, no. 2, pp. 640–645, Feb. 2020.

[10] X. Han, Q. Mao, L. Zhao, X. Li, L. Wang, P. Yang, D. Lu, Y. Wang, X. Yan, S. Wang, N. Zhu, and Z. Jiang, "Novel resonant pressure sensor based on piezoresistive detection and symmetrical in-plane mode vibration," *Microsystems & Nanoengineering*, vol. 6, no. 1, p. 95, Dec. 2020.

[11] N. Alcheikh, S. Ben. Mbarek, H. Ouakad, and M. Younis, "A highly sensitive and wide-range resonant magnetic micro-sensor based on a buckled micro-beam," *Sensors and Actuators A: Physical*, vol. 328, p. 112768, Sep. 2021.

[12] Y. Wang, X. Song, F. Li, L. Gao, C. Li, J. Xi, H. Liu, C. Zhao, C. Wang, L.-C. Tu, and M. Kraft, "A Resonant Lorentz-Force Magnetometer Featuring Slotted Double-Ended Tuning Fork Capable of Operating in a Bias Magnetic Field," *Journal of Microelectromechanical Systems*, vol. 30, no. 6, pp. 958–967, 2021.

[13] C. Li, J. Xi, Y. Wang, F. Li, L. Gao, H. Liu, C. Zhao, and L.-C. Tu, "On Enhancing the Sensitivity of Resonant Thermometers Based on Parametric Modulation," *Journal of Microelectromechanical Systems*, vol. 30, no. 4, pp. 539–549, 2021.

[14] X. Zou, S. Ahmed, N. Jaber, and H. Fariborzi, "A Compact High-Sensitivity Temperature Sensor using an Encapsulated Clamped-Clamped MEMS Beam Resonator," in *2021 21st International Conference on Solid-State Sensors, Actuators and Microsystems (Transducers)*. Orlando, FL, USA: IEEE, Jun. 2021, pp. 1239–1242.

[15] G. Langfelder, M. Bestetti, and M. Gadola, "Silicon MEMS inertial sensors evolution over a quarter century," *Journal of Micromechanics and Microengineering*, vol. 31, no. 8, p. 084002, jul 2021.

[16] X. Wang, J. Zhao, Y. Zhao, G. M. Xia, A. P. Qiu, Y. Su, and Y. P. Xu, "A 0.4-μg bias instability and 1.2μg/rthz noise floor MEMS silicon oscillating accelerometer with CMOS readout circuit," *IEEE Journal of Solid-State Circuits*, vol. 52, no. 2, pp. 472–482, Feb. 2017.

[17] M. Pandit, G. Sobreviela, C. Pili, P. Steinmann, D. Young, C. Zhao, C. Baker, and A. Seshia, "A 10 ng/rt-Hz Resonant MEMS Accelerometer Employing Anti-aliasing Control," in *2021 IEEE International Symposium on Inertial Sensors and Systems (INERTIAL)*. Kailua-Kona, HI, USA: IEEE, Mar. 2021, pp. 1–4.

[18] G. Langfelder, A. Caspani, and A. Tocchio, "Design Criteria of Low-Power Oscillators for Consumer-Grade MEMS Resonant Sensors," *IEEE Transactions on Industrial Electronics*, vol. 61, no. 1, pp. 567–574, 2014.

[19] J. Van Beek and R. Puers, "A review of MEMS oscillators for frequency reference and timing applications," *Journal of Micromechanics and Microengineering*, vol. 22, no. 1, p. 013001, 2011.

[20] L. G. Villanueva, R. B. Karabalin, M. H. Matheny, E. Kenig, M. C. Cross, and M. L. Roukes, "A nanoscale parametric feedback oscillator," *Nano letters*, vol. 11, no. 11, pp. 5054–5059, 2011.

[21] G. Sobreviela, C. Zhao, M. Pandit, C. Do, S. Du, X. Zou, and A. Seshia, "Parametric noise reduction in a high-order nonlinear MEMS resonator utilizing its bifurcation points," *Journal of Microelectromechanical Systems*, vol. 26, no. 6, pp. 1189–1195, 2017.

[22] L. Gaffuri Pagani, L. Guerinoni, L. Falorni, P. Fedeli, P. Carulli, and G. Langfelder, "Direct Phase Measurement and Compensation to Enhance MEMS Gyroscopes ZRO Stability," *Journal of Microelectromechanical Systems*, vol. 30, no. 5, pp. 703–711, 2021.

[23] M. Zalalutdinov, A. Zehnder, A. Olkhovets, S. Turner, L. Sekaric, B. Ilic, D. Czaplewski, J. Parpia, and H. Craighead, "Autoparametric optical drive for micromechanical oscillators," *Applied Physics Letters*, vol. 79, no. 5, pp. 695–697, jul 2001.

[24] K. Usami, A. Naesby, T. Bagci, B. Nielsen, J. Liu, S. Stobbe, P. Lodahl, and E. Polzik, "Optical cavity cooling of mechanical modes of a semiconductor nanomembrane," *Nature Physics*, vol. 8, no. 2, pp. 168–172, jan 2012.

[25] E. Gil-Santos, M. Labousse, C. Baker, A. Goetschy, W. Hease, C. Gomez, A. Lemaître, G. Leo, C. Ciuti, and I. Favero, "Light-Mediated Cascaded Locking of Multiple Nano-Optomechanical Oscillators," *Physical Review Letters*, vol. 118, p. 063605, Feb 2017.

[26] H. Rokhsari, T. J. Kippenberg, T. Carmon, K. J. Vahala, "Theoretical and experimental study of radiation pressure-induced mechanical oscillations (parametric instability) in optical microcavities," *IEEE Journal of Selected Topics in Quantum Electronics*, vol. 12, no. 1, pp. 96–107, 2006.

[27] A. Olkhovets, D. Carr, J. Parpia, and H. Craighead, "Non-degenerate nanomechanical parametric amplifier," in *Technical Digest. MEMS 2001. 14th IEEE International Conference on Micro Electro Mechanical Systems (Cat. No.01CH37090)*. Interlaken, Switzerland: IEEE, 2001, pp. 298–300.

[28] R. Baskaran and K. L. Turner, "Mechanical domain coupled mode parametric resonance and amplification in a torsional mode micro electro mechanical oscillator," *Journal of Micromechanics and Microengineering*, vol. 13, no. 5, pp. 701–707, Sep. 2003.

[29] W. J. Venstra, H. J. R. Westra, and H. S. J. van der Zant, "Q-factor control of a microcantilever by mechanical sideband excitation," *Applied Physics Letters*, vol. 99, no. 15, p. 151904, Oct. 2011.

[30] I. Mahboob, H. Okamoto, K. Onomitsu, and H. Yamaguchi, "Two-Mode Thermal-Noise Squeezing in an Electromechanical Resonator," *Physical Review Letters*, vol. 113, no. 16, p. 167203, Oct. 2014.

[31] X. Dong, M. I. Dykman, and H. B. Chan, "Strong negative nonlinear friction from induced two-phonon processes in vibrational systems," *Nature Communications*, vol. 9, no. 1, p. 3241, Dec. 2018.

[32] T. Miao, X. Hu, X. Zhou, X. Wu, Z. Hou, and D. Xiao, "A Million-order Effective Quality Factor MEMS Resonator by Mechanical Pumping," in *2020 IEEE International Symposium on Inertial Sensors and Systems (INERTIAL)*. Hiroshima, Japan: IEEE, Mar. 2020, pp. 1–4.

[33] G. Pillai and S.-S. Li, "Controllable multichannel acousto-optic modulator and frequency synthesizer enabled by nonlinear MEMS resonator," *Scientific reports*, vol. 11, no. 1, pp. 1–13, 2021.

[34] C. M. Bender and S. A. Orszag, *Advanced mathematical methods for scientists and engineers I: Asymptotic methods and perturbation theory*. Springer Science & Business Media, 2013.

[35] A. H. Nayfeh, D. T. Mook, and P. Holmes, "Nonlinear oscillations," 1980.

[36] X. Zhou, C. Zhao, D. Xiao, J. Sun, G. Sobreviela, D. D. Gerrard, Y. Chen, I. Flader, T. W. Kenny, X. Wu *et al.*, "Dynamic modulation of modal coupling in microelectromechanical gyroscopic ring resonators," *Nature communications*, vol. 10, no. 1, pp. 1–9, 2019.

[37] C. Zhao, X. Zhou, M. Pandit, G. Sobreviela, S. Du, X. Zou, and A. Seshia, "Toward high-resolution inertial sensors employing parametric modulation in coupled micromechanical resonators," *Physical Review Applied*, vol. 12, no. 4, p. 044005, 2019.

[38] H. Zhang, D. Chen, M. Pandit, J. Sun, C. Zhao, and A. Seshia, "Amplitude-modulated resonant accelerometer employing parametric pump," *Applied Physics Letters*, vol. 117, no. 16, p. 163504, 2020.

[39] J. Miller, D. D. Shin, H. K. Kwon, S. W. Shaw, T. W. Kenny, "Phase Control of Self-Excited Parametric Resonators," *Physical Review Applied*, vol. 12, no. 4, p. 044053, oct 2019.

[40] M. Heidarpour Roshan, S. Zaliasl, K. Joo, K. Souri, R. Palwai, L. W. Chen, A. Singh, S. Pamarti, N. J. Miller, J. C. Doll, C. Arft, S. Tabatabaei, C. Sechen, A. Partridge, and V. Menon, "A MEMS-Assisted Temperature Sensor With 20- μK Resolution, Conversion Rate of 200 S/s, and FOM of 0.04 pJK2," *IEEE Journal of Solid-State Circuits*, vol. 52, no. 1, pp. 185–197, Jan. 2017.

[41] J. Zhao, X. Wang, Y. Zhao, G. M. Xia, A. P. Qiu, Y. Su, and Y. P. Xu, "A 0.23- μg Bias Instability and 1- $\mu g/\sqrt{}$ Hz Acceleration Noise Density Silicon Oscillating Accelerometer With Embedded Frequency-to-Digital Converter in PLL," *IEEE Journal of Solid-State Circuits*, vol. 52, no. 4, pp. 1053–1065, Apr. 2017.

[42] E. Bordiga, M. Bestetti, and G. Langfelder, "AGC-Less Operation of High-Stability Lissajous Frequency-Modulated MEMS Gyroscopes," in *2019 20th International Conference on Solid-State Sensors, Actuators and Microsystems Eurosensors XXXIII (TRANSDUCERS EUROSENSORS XXXIII)*, 2019, pp. 594–597.

[43] X. Wang, J. Zhao, Y. Zhao, G. M. Xia, A. P. Qiu, Y. Su, and Y. P. Xu, "A 0.4 μg Bias Instability and 1.2 $\mu g/\sqrt{}$ Hz Noise Floor MEMS Silicon Oscillating Accelerometer With CMOS Readout Circuit," *IEEE Journal of Solid-State Circuits*, vol. 52, no. 2, pp. 472–482, 2017.

[44] M. Pandit, A. Mustafazade, C. Zhao, G. Sobreviela, X. Zou, P. Steinmann, and A. Seshia, "An ultra-high resolution resonant MEMS accelerometer," in *2019 IEEE 32nd International Conference on Micro Electro Mechanical Systems (MEMS)*. IEEE, 2019, pp. 664–667.

[45] Y. Zheng, S. Zhang, D. Chen, J. Wang, and J. Chen, "A Micromachined Resonant Low-Pressure Sensor With High Quality Factor," *IEEE Sensors Journal*, vol. 21, no. 18, pp. 19 840–19 846, 2021.

[46] Y. Wang, X. Song, J. Xi, F. Li, L. Xu, H. Liu, C. Wang, S. Kuang, L.-C. Tu, M. Kraft *et al.*, "A Resonant Lorentz-Force Magnetometer Exploiting Blue Sideband Actuation to Enhance Sensitivity and Resolution," *Journal of Microelectromechanical Systems*, 2022.

[47] C. H. Ahn, E. J. Ng, V. A. Hong, Y. Yang, B. J. Lee, I. Flader, and T. W. Kenny, "Mode-matching of wineglass mode disk resonator gyroscope in (100) single crystal silicon," *Journal of Microelectromechanical Systems*, vol. 24, no. 2, pp. 343–350, 2014.

[48] Y. Yang, E. Ng, P. Polunin, Y. Chen, S. Strachan, V. Hong, C. H. Ahn, O. Shoshani, S. W. Shaw, M. I. Dykman, T. W. Kenny, "Experimental investigation on mode coupling of bulk mode silicon MEMS resonators," in *2015 28th IEEE International Conference on Micro Electro Mechanical Systems (MEMS)*. IEEE, 2015, pp. 1008–1011.

[49] Y. Wang, C. Zhao, C. Wang, D. Cerica, M. Baijot, Q. Xiao, S. Stoukatch, and M. Kraft, "A mass sensor based on 3-DOF mode localized coupled resonator under atmospheric pressure," *Sensors and Actuators A: Physical*, vol. 279, pp. 254–262, 2018.

[50] M. Manav, A. S. Phani, and E. Cretu, "Mode localization and sensitivity in weakly coupled resonators," *IEEE Sensors Journal*, vol. 19, no. 8, pp. 2999–3007, 2018.

[51] J. Juillard, A. Mostafa, and P. M. Ferreira, "Nonlinear operation of resonant sensors based on weakly coupled resonators: Theory and modeling," *IEEE Transactions on Ultrasonics, Ferroelectrics, and Frequency Control*, vol. 66, no. 12, pp. 1950–1961, 2019.

[52] T. Liu, P. C.-P. Chao, and B. Choubey, "Enhanced sensory identification in arrays of coupled resonant sensors," *IEEE Sensors Journal*, 2022.

[53] H. Zhang, M. Pandit, G. Sobreviela, M. Parajuli, D. Chen, J. Sun, C. Zhao, and A. A. Seshia, "Mode-localized accelerometer in the nonlinear Duffing regime with 75 ng bias instability and 95 ng/Hz$^{1/2}$ noise floor," *Microsystems & nanoengineering*, vol. 8, no. 1, pp. 1–11, 2022.

[54] T. Zhang, J. Ren, X. Wei, Z. Jiang, and R. Huan, "Nonlinear coupling of flexural mode and extensional bulk mode in micromechanical resonators," *Applied Physics Letters*, vol. 109, no. 22, p. 224102, 2016.